## PAPER

Check for updates

# MIL-101-SO₃H: functionalized MOF for enhanced barium ion adsorption and environmental remediation

Abouzar Tahkor,[a] Seyed Dariush Taherzade, [iD] *[bc] Niloufar Akbarzadeh,[a] Alireza Rezvani[a] and Janet Soleimannejad*[b]

Cationic pollution from barium ions in wastewater poses environmental and health risks including cardiovascular effects and disrupted aquatic ecosystems. This study investigates the use of Metal–Organic Frameworks (MOFs), including both MIL-101(Cr) and its sulfonated derivative MIL-101-SO₃H, for efficient removal of barium ions in contaminated water sources. Sulfonation of MIL-101 at the metal center was shown to considerably increase its adsorption capacity compared to unmodified MIL-101 for barium ions, achieving 141.9 mg g$^{-1}$ for Ba$^{2+}$ as compared to 54 mg g$^{-1}$ for MIL-101. The study deeply looked into the effects of the pH, adsorbent dosage, initial Ba$^{2+}$ concentration, and contact time on adsorption efficiency. Approximately pH = 4 has been determined as the best for Ba$^{2+}$ adsorption at which the sulfonated MOF gave essentially complete removal efficiencies of 99% of the barium cations. The adsorption correlated with the Langmuir model indicates a homogeneous monolayer adsorption on the surface. MIL-101-SO₃H, given the superior characteristics of its adsorptive ability compared with other materials including MIL-101, is tested with ion coexistence and retention trials. These results indicate that MIL-101-SO₃H would be an extremely efficient adsorbent for barium ion removal from wastewater that could prove beneficial for a future large-scale application in environmental remediation.

## Introduction

Cationic pollution of wastewater with barium ions is one of the biggest environmental concerns due to their toxicity and possible health hazards.[1,2] High levels of this metal result in cardiovascular problems, hypertension, and other harmful effects in humans upon ingestion through contaminated water.[3] Besides, barium interferes with aquatic life by breaking the ionic balance in water bodies.[3] In light of this, the effective removal of barium from wastewater is a key concern for both environmental and human health requirements.[4–6] Metal–Organic Frameworks (MOFs) have the potential to change this landscape owing to their incredible porosity,[7] adjustable properties,[8] and their various applications. Such properties make MOFs very suitable for a plethora of applications including gas storage,[9] separation,[10] catalysis[11] and also wastewater remediation.[12,13] Thus, the employment of MOFs is one important green and very efficient method for elimination of barium from wastewater.[14,15] The MOF family of materials called Materials of

Institute Lavoisier (MIL) is a family of materials with desirable structural stability, porosity and tunability.[16,17] Most of these MOFs are made from metals such as aluminum,[18] iron,[19] and chromium,[20] and linkers such as terephthalic acid[21] that create a volumetric structure with high porosity. A number of them, such as MIL-53,[17] MIL-88,[19] MIL-101 (ref. 20) demonstrate diverse structural features and functionality.

Among the abovementioned MILs, MIL-101(Cr) is known for its fascinating layer structure and high industrial value.[22,23] MIL-101(Cr) has an unusual large cavity system with two different kinds of mesopores, providing high surface area and large volume of pores which enhance its adsorption tendency.[24,25] The material showcases outstanding stability to elevated temperatures as well as to many different chemicals, alongside considerable freedom in the envisaged structural plan which can be further modified through changing the organic linkers or the metal centers.[26] This makes MIL-101(Cr) very useful in a variety of applications such as gas storage,[27] catalysis[28] or separation.[16] Moreover, the material with large pores and a high surface area allows for incorporation of a range of guest molecules, opening up its application for environmental cleaning[29–31] among others in advanced material science.

This article describes MIL-101(Cr) in detail, including its preparation, properties, and modification, as well as its sulfonated form, MIL-101-SO₃H, which is designed to improve the functional properties of this framework for different

[a]Department of Chemistry, University of Sistan and Baluchestan, P. O. Box 98135-674, Zahedan, Iran

[b]School of Chemistry, College of Science, University of Tehran, P. O. Box 14155-6455, Tehran, Iran. E-mail: jsoleimannejad@ut.ac.ir

[c]College of Materials Science and Engineering, Hunan University, 2 Lushan S Rd, Changsha, 410082, PR China. E-mail: d.taherzade@hnu.edu.cn

advanced applications. To the best of our knowledge, in most cases, sulfonation is used to modify the organic linkers within MOFs, which is because sulfonate groups bonded to the linkers improve the hydrophilicity and ion-exchange capacity as well as the catalytic activity.[32,33] In this work however, we consider an alternative way using sulfonate functional group covalent attachment to metal centers of MIL-101(Cr). This strategy introduces a new approach of improving the functionalities of MOFs by looking at the metal nodes. This can potentially lead to the development of new materials with specific interactions with ions that are required in their applications. Not only the previous reports, but also the current study indicates that the node-functionalization influences the adsorption and desorption efficiencies of the material, especially speaking about bivalent cations, like barium cations.[34,35] These studies pave the way for a variety of new applications of MIL-101-SO$_3$H, including environmental and catalytic applications where selective capture and release of ions is likely to be critical. After gaining the knowledge of the design, development, and alteration of these structures, this paper opens the door to the exploration of the applicability of functionalized MOFs across several industries, the environment, and for catalytic purposes.

## Experimental section

### Materials and instruments

The reactants and solvents were acquired from commercial sources and utilized without additional purification. Fourier transforms infrared (FT-IR) spectra were obtained using a Bruker Tensor II spectrometer, which was coupled with a single reflection ATR system. The catalysts were examined *via* field emission scanning electron microscopy (FE-SEM) on a KYKY EM3900M instrument with a SE detector. X-ray diffraction (XRD) patterns were obtained using a Bruker Advance D8 diffractometer, operated at 40 kV and 30 mA utilizing Cu-K$\alpha$ radiation ($\lambda = 1.5406$ Å) within the $2\theta$ range of 4–80°. The surface area and pore volume of the samples were determined by nitrogen adsorption/desorption measurements using a Belsorp-mini gas analyzer from MicrotracBel Corp. company at liquid nitrogen temperature. Prior to the adsorption experiments, the samples were degassed under vacuum at 150 °C for 12 h. Thermogravimetric analysis (TGA) was performed utilizing a TGA/DTA (STA 504) instrument from Bahr Company, where the samples were heated from 50 to 700 °C in air at a constant rate of 20 °C min$^{-1}$. For X-ray Photoelectron Spectroscopy (XPS) analysis, a SPECS UHV analysis system (Germany) was used to acquire the spectra of the samples.

### Synthesis of MIL-101(Cr)

Synthesis of the MIL-101(Cr) was carried out as previously described in the literature,[36] with some modifications. In this case, 3 mmol (0.5 g) of terephthalic acid ligand were mixed with 3 mmol (1.2 g) of chromium(III) nitrate nonahydrate in a 25 mL autoclave. Then 0.6 mL of 5 M hydrofluoric acid was added to the mixture as a catalyst. This solution was topped up with 15 mL of distilled water, put into the autoclave, and maintained

at a temperature of 220 °C for 8 hours. Temperature program was implemented to allow the increase in the room temperature to 220 °C over 4 hours. After 8 hours, the autoclave was allowed to cool to ambient temperature for 24 hours, then it was removed from the oven. The resulting green precipitate of MIL-101(Cr) was collected *via* centrifugation and subsequently refluxed in DMF for 3 hours at 60 °C, followed by reflux in ethanol for 2.5 hours at 70 °C. The final precipitate was then dried in an oven at 70 °C following the filtration process.

### Synthesis of MIL-101(Cr)-SO$_3$H

The MIL-101(Cr)-SO$_3$H was prepared by using the procedure described in earlier reports.[37] The synthesis started with 2 mmol cysteamine hydrochloride and 2 mmol NaOH dissolved in 20 mL of hot absolute ethanol, followed by stirring of the solution to displace hydrochloride. The forming NaCl was separated by centrifugation, and the supernatant was combined with 1 g of dehydrated MIL-101(Cr) in 20 mL ethanol in a round bottom flask, which was then refluxed for 16 hours. The mixture was subsequently filtered and washed twice with deionized water and ethanol, followed by drying at 80 °C for twelve hours. Then, the thiol groups of MIL-101(Cr)-SO$_3$H were oxidized with hydrogen peroxide and sulfonic acid groups were introduced. In a typical experiment, 0.5 g of MIL-101(Cr)-SO$_3$H was dispersed in a water : ethanol (1 : 1) mixture with stirring, and treated with 10 mL of H$_2$O$_2$ (1% weight) solution for 24 hours at room temperature. The product was collected by filtration, washed with ethanol and deionized water, and then stirred in 0.1 M H$_2$SO$_4$ for four hours. Finally, MIL-101(Cr)-SO$_3$H was thoroughly rinsed with deionized water and ethanol and finally placed in a vacuum at 120 °C for drying.

### Adsorption experiment

In this study, batch experiments were conducted by adding 10 mL of aqueous solution containing specific concentrations of barium to a specific amount of MOFs. The impact of varying initial barium concentrations from 50 ppm (mg L$^{-1}$) to 200 ppm on adsorption capacity and removal efficiency was evaluated. Equilibrium studies were performed at different time intervals, with a maximum time of 360 min to determine the equilibrium contact time and capacity. To determine the optimal amount of MOF for maximum removal of barium from water, different amounts ranging from 10 and 50 mg were tested. The dependency of barium removal efficiency on pH was studied by conducting experiments at different pH values ranging from 3 to 11. To achieve the desired pH, acid or base was added drop by drop after measuring the initial pH of the solution. All experiments were conducted in triplicate, and the average values are reported.

It should be noted that in this study, nonradioactive Ba$^{2+}$ was utilized instead of radioactive $^{133}$Ba$^{2+}$ in all experiments. To perform the adsorption experiments, 10 mg of the adsorbent was added to a 10 mL Ba$^{2+}$ solution and mixed using a constant temperature shaker. The resulting solution was then filtered to obtain a clear filtrate which was analyzed for its concentration

using an ICP-OES spectrometer. The amount of $Ba^{2+}$ adsorbed was determined using the following equation:

$$Q = \frac{(C_0 - C_e) \times V}{m} \qquad (1)$$

where $C_0$ (mg L$^{-1}$) and $C_e$ (mg L$^{-1}$) are the initial and final concentrations of metal ions, $V$ (L) is the solution volume and $m$ (g) are the adsorbent mass, $Q$ (mg g$^{-1}$) refers to the adsorption amount.

### Adsorption kinetics study

The kinetics of $Ba^{2+}$ adsorption were further assessed. The experimental data were analyzed according to the pseudo-first-order and pseudo-second-order models. The linear forms of these equations are given by eqn (2) (pseudo-first-order) and eqn (3) (pseudo-second-order).

$$\ln(Q_e - Q_t) = \ln \quad Q_e - k_1 t \qquad (2)$$

$$\frac{t}{Q_t} = \frac{1}{k_2 Q_e^2} + \frac{t}{Q_e} \qquad (3)$$

The pseudo-first-order and pseudo-second-order models yielded the adsorption capacity $Q_t$ of $Ba^{2+}$ at time $t$, whereby $k_1$ is the first-order rate constant and $k_2$ is the second-order rate constant.

### Adsorption mechanism study

The Freundlich and Langmuir isotherm models were employed to determine the maximum adsorption capacity and sorption energy of barium on adsorbents. The resulting linear mathematical expressions for these models are given below.

$$\ln Q_e = \ln K_F + \frac{1}{n} \ln C_e \qquad (4)$$

$$\frac{C_e}{Q_e} = \frac{1}{X_m K} + \frac{C_e}{X_m} \qquad (5)$$

Eqn (4) and (5) were utilized to describe the barium adsorption capacity on the adsorbent. Eqn (4) corresponds to the Freundlich isotherm model and gives the relationship between $C_e$, $Q_e$, and the Freundlich empirical constants, $K_F$ and $n$. $K_F$ signifies the sorption capacity of the adsorbent while $n$ represents the intensity of sorption. The Langmuir isotherm model was expressed by eqn (5) which relates the maximum adsorption capacity, $X_m$ (mg g$^{-1}$), and the Langmuir equilibrium constant, $K$, to $C_e$.

### Selectivity test

To assess how much MIL-101-SO$_3$H can selectively adsorb $Ba^{2+}$ ions in a multi cation environment, competitive adsorption studies were performed. These studies focused on how these competing co ions, $Cr^{2+}$, $Ni^{2+}$, $Co^{2+}$, and $Zn^{2+}$, would affect the adsorption of $Ba^{2+}$. The interfering ions were all obtained by the dissolution of their respective nitrate salts in deionized water at 10 mg L$^{-1}$ concentrations. $Ba^{2+}$ was prepared separately at

10 mg L$^{-1}$ concentration. All solutions were adjusted to the desired pH range of 6 to 7 by dilute HCl or NaOH. For each competitive adsorption study, 10 mg of MIL-101-SO$_3$H was dispersed in 10 mL $Ba^{2+}$ solution with those of the coexisting metal ions to agitate at 200 rpm for 360 minutes at room temperature (25 ± 2 °C) in constant temperature shaker. Then, the suspensions were filtered through a 0.45 micrometer membrane filter to obtain the clear filtrates. The amounts of $Ba^{2+}$ and the interfering metal ions present in the filtrate were quantified using ICP-OES. The effectiveness of MIL-101-SO$_3$H in removing $Ba^{2+}$ in the presence of competing ions was then determined and compared. The selectivity coefficient was determined to assess the affinity of MIL-101-SO$_3$H toward $Ba^{2+}$ relative to the interfering cations. The data obtained were analyzed for the contribution of sulfonic acid (–SO$_3$H) functional groups toward the selectivity of adsorption of $Ba^{2+}$.

## Results and discussion

### Characterization

**XRD pattern.** As depicted in Fig. 1a, the XRD pattern of MIL-101 has a series of sharp peaks well separated from one another; it is an indication of the high crystalline nature of this compound. The most prominent peaks, along with their corresponding crystallographic planes, include: (1) a strong peak at $2\theta \sim 5°$ corresponding to the (100) plane, (2) a peak at $2\theta \sim 8.0°$ corresponding to the (200) plane, (3) another strong peak at $2\theta \sim 10°$ corresponding to the (210) plane, and (4) a peak at $2\theta \sim 17°$ corresponding to the (211) plane. Such characteristic peaks are following the reported XRD pattern of the structure of MIL-101, thus confirming the formation of the desired crystalline framework.[24]

The XRD pattern of MIL-101-SO$_3$H shows roughly the same diffraction pattern compared to pristine MIL-101, inferring that the sulfonation process does not remarkably affect the overall crystalline structure of the material. The XRD pattern of MIL-101(Cr)-SO$_3$H still shows some of the characteristic peaks of MIL-101. However, there might be a slight displacement or broadening of these peaks, which will be indicative that the introduction of sulfonate groups is likely to have a minor effect on interplanar spacing or the lattice parameters. The changes in the X-ray diffraction pattern are minor and are consistent with sulfonate groups that are directly tied to the Cr unsaturated sites in the framework and only slightly change local structure without disrupting the overall crystallographic framework.[38,39]

**FT-IR spectra.** The FT-IR spectrum of MIL-101 exhibits characteristic peaks that provide insights into its structural features, as illustrated in Fig. 1b. In the range of 400–500 cm$^{-1}$, a strong band corresponds to the metal–oxygen (Cr–O) stretching vibrations within the octahedral Cr(III) units that form the framework. The region between 1350 and 1650 cm$^{-1}$ is dominated by the presence of carboxylate groups, with peaks around 1580 cm$^{-1}$ and 1380 cm$^{-1}$ attributed to the asymmetric and symmetric stretching modes of the carboxylate groups, respectively. These peaks indicate the coordination of the carboxylate groups to the chromium ions, forming the characteristic framework structure of MIL-101. Additionally, the
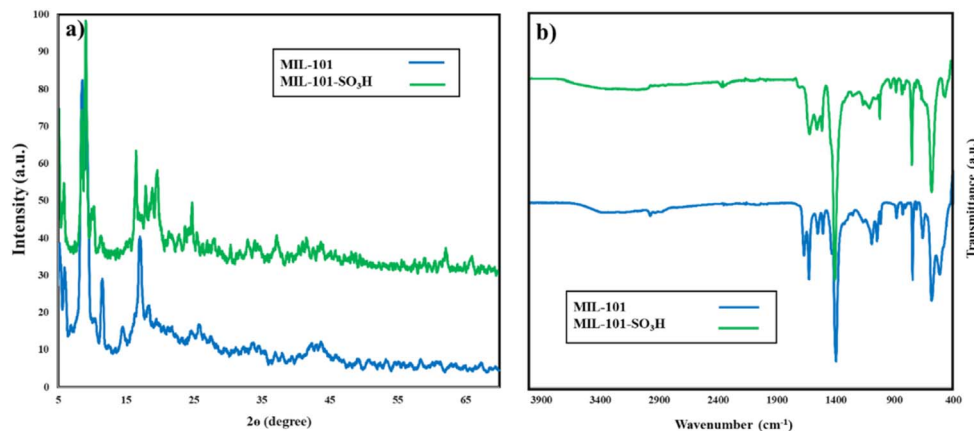
**Fig. 1** XRD patterns (a) and FT-IR spectra (b) of MIL-101 and MIL-101-SO$_3$H.

presence of benzene groups is evident by the peak at approximately 1420 cm$^{-1}$, corresponding to the C–H bending vibrations of the aromatic ring.[40] These spectral features collectively confirm the successful synthesis of MIL-101 and provide a fingerprint for identifying its structural integrity.

The FT-IR spectrum of MIL-101-SO$_3$H shows distinct changes, which already confirm that the MIL-101 framework underwent sulfonation. Prominent changes were noted within the wavenumber range of 1000–1200 cm$^{-1}$, wherein several strong peaks emerged around 1170 cm$^{-1}$. These peaks are used to identify the asymmetric and symmetric stretching vibrations of the S=O bonds found in the sulfonic acid group (SO$_3$H). The

presence of these peaks confirms the successful incorporation of sulfonate groups onto the MIL-101 structure. Additionally, the peak around 1120 cm$^{-1}$ attributed to the S–O stretching vibrations further supports the presence of sulfonate groups. These spectral modifications demonstrate the successful functionalization of MIL-101 with SO$_3$H groups, resulting in the formation of MIL-101-SO$_3$H with enhanced acidic properties.

**SEM.** Distinct morphologies of MIL-101 and MIL-101-SO$_3$H observed from the SEM images shed some light on the sulfonation-induced structural changes. MIL-101(Cr) shows a characteristic well-defined octahedral morphology masking any irregularity, typical of a crystalline material. Some signs of
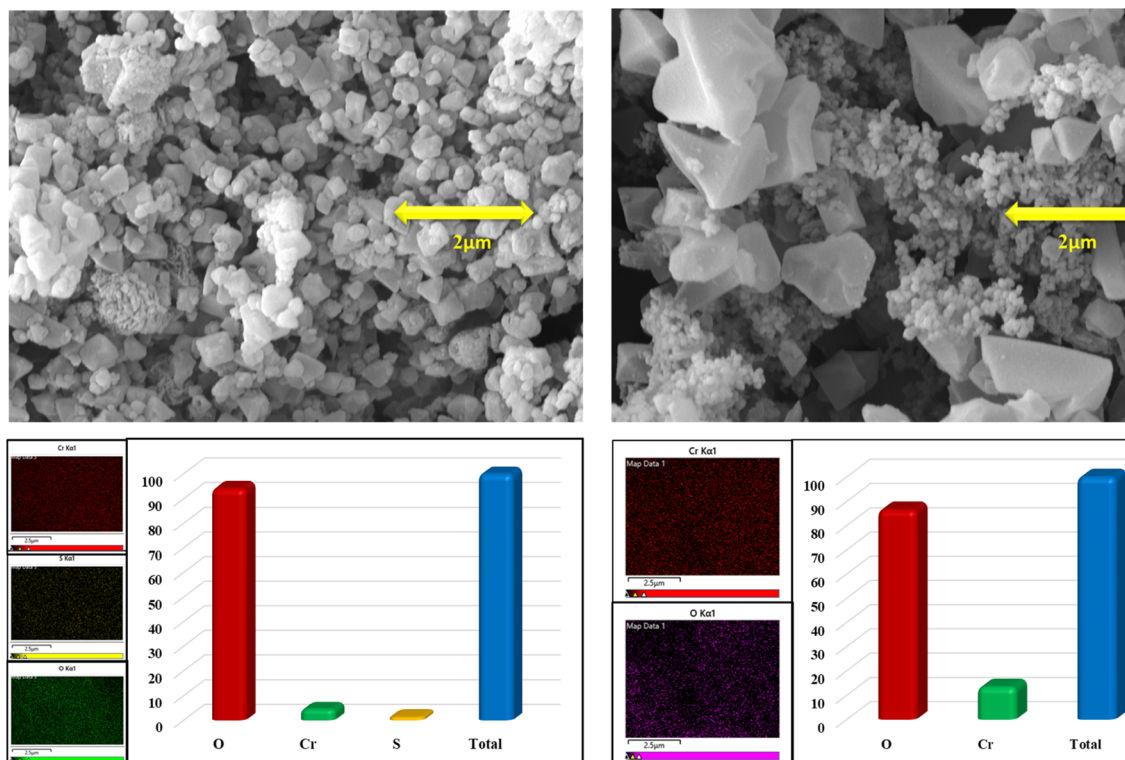


**Fig. 2** The SEM images and EDS-mapping of MIL-101-SO$_3$H (left) and MIL-101 (right).

altered morphology in the surface of less defined octahedral shapes can be observed in MIL-101-SO$_3$H. This change in morphology can be attributed to the incorporation of sulfonate groups onto the framework, potentially leading to a subtle rearrangement of the structure and a less defined octahedral morphology. EDS-mapping of both materials confirms the presence of the expected elements: Cr and O for MIL-101, and Cr, O, and S for MIL-101-SO$_3$H. The mapping for MIL-101-SO$_3$H displays the presence of sulfur, confirming the successful incorporation of sulfonate groups within the material's structure. This evidence, combined with the morphological changes observed through SEM, provides further support for the successful sulfonation of MIL-101 and highlights the impact of this functionalization on the material's morphology and elemental composition. Fig. 2 provides the SEM images and EDS-mapping results of both MOFs.

**BET analysis.** The N$_2$ adsorption–desorption isotherms of MIL-101(Cr) and MIL-101(Cr)-SO$_3$H reveal different characteristics, which serve to demonstrate how sulfonation affects porosity of those two materials (Fig. 3). Both isotherms exhibit type II behavior, typical of mesoporous materials, with a sharp increase in nitrogen uptake at low relative pressures, indicating a high density of mesopores. However, a notable difference emerges in the overall nitrogen uptake capacity and pore volume between the two materials. MIL-101 exhibits a significantly higher nitrogen uptake compared to MIL-101-SO$_3$H,

indicating a greater surface area and pore volume. The BET surface area of MIL-101 is measured as 2055.4 m$^2$ g$^{-1}$, while its total pore volume is 0.9614 cm$^3$ g$^{-1}$. In contrast, MIL-101-SO$_3$H shows a reduced BET surface area of 1302.8 m$^2$ g$^{-1}$ and a lower total pore volume of 0.7617 cm$^3$ g$^{-1}$. The decrease in surface area and pore volume after sulfonation can be explained via the blockages of some mesopores caused by the introduction of bulky sulfonate groups on the framework, so the overall accessible surface area and pore volume will also be reduced. The degree of decrease in surface area and pore volume indicates that the sulfonation greatly influences the textural properties of the material, which will surely affect its adsorption capacity and accessibility towards various molecules.

**TGA analysis.** The TGA curves of MIL-101 and MIL-101-SO$_3$H show the thermal stability and how sulfonation affects the decomposition. Both materials exhibit a similar initial weight loss up to approximately 120 °C, attributed to the loss of adsorbed solvent molecules. However, the sulfonated analogue, MIL-101-SO$_3$H, shows a more gradual weight loss over a broader temperature range compared to the pristine MIL-101(Cr). This difference is likely due to the presence of sulfonate groups, which contribute additional organic moieties to the material. The increased organic content in MIL-101-SO$_3$H leads to a higher overall weight loss during thermal decomposition. Consequently, the inorganic residue remaining after decomposition is lower in the sulfonated material compared to the
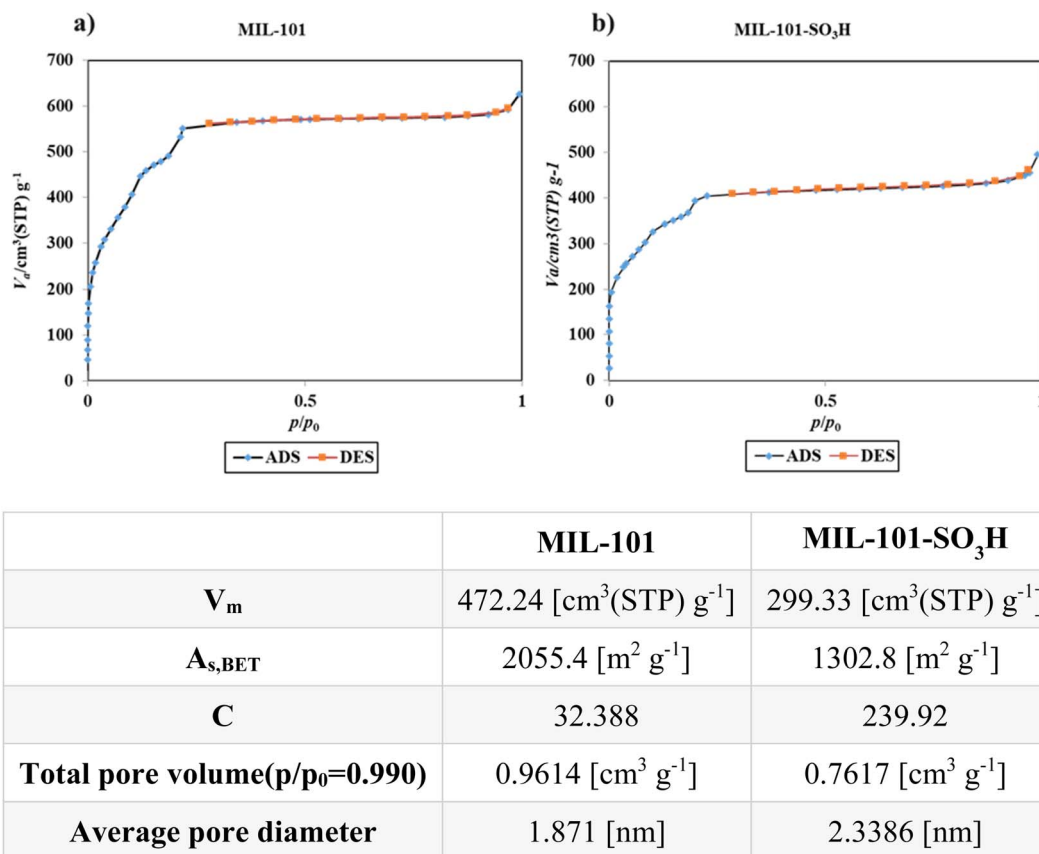


| | **MIL-101** | **MIL-101-SO$_3$H** |
|---|---|---|
| **V$_m$** | 472.24 [cm$^3$(STP) g$^{-1}$] | 299.33 [cm$^3$(STP) g$^{-1}$] |
| **A$_{s,BET}$** | 2055.4 [m$^2$ g$^{-1}$] | 1302.8 [m$^2$ g$^{-1}$] |
| **C** | 32.388 | 239.92 |
| **Total pore volume(p/p$_0$=0.990)** | 0.9614 [cm$^3$ g$^{-1}$] | 0.7617 [cm$^3$ g$^{-1}$] |
| **Average pore diameter** | 1.871 [nm] | 2.3386 [nm] |

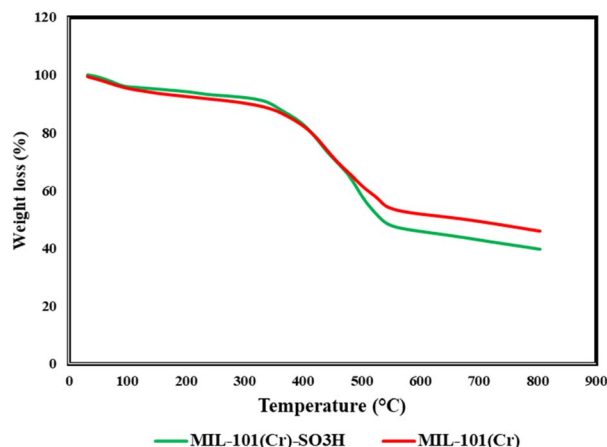**Fig. 3** N$_2$ adsorption–desorption of MIL-101 (a) and MIL-101-SO$_3$H (b).

**Fig. 4** TGA curves of MIL-101 (red) and MIL-101-SO$_3$H (green).

pristine MIL-101. The TGA analysis, as shown in Fig. 4, confirms that the sulfonation process introduces extra organic components into the framework, which affects the thermal stability and decomposition profile of the material.

**DLS and zeta potential.** The zeta potential of MIL-101 and MIL-101-SO$_3$H shows the introduction of sulfonate groups and their effect on the surface charge of the material. At pH ~5, MIL-101 has a zeta potential of −9.60 mV, slightly negative surface charge which is due to deprotonation of carboxylate groups (–COO$^-$) in the framework. MIL-101-SO$_3$H has a zeta potential of +1.31 mV at the same pH. The positive shift in zeta potential is due to sulfonation of the framework which introduces sulfonate groups (–SO$_3$H). These sulfonate groups, when protonated in the given pH range, neutralize some of the deprotonated groups and reduce the negative surface charge to a less negative or positive surface charge. The big change in zeta potential shows the successful introduction of sulfonate groups and how they can tune the surface charge and electrostatic interactions of the MOF material. Fig. 5 shows the zeta potential values of both materials.

The collected characterization data (XRD patterns, FT-IR spectra, and TGA profiles) for MIL-101(Cr) show excellent agreement with previously reported results, confirming the successful synthesis of the parent framework.[26,36,41] Similarly, the modified MIL-101-SO$_3$H material demonstrates all expected functional group vibrations in FT-IR, while maintaining the parent framework's thermal stability in TGA.[37] These collective results verify both the preservation of the MIL-101 structure during functionalization and the successful incorporation of sulfonic acid groups, consistent with literature reports.

### Adsorption of Ba$^{2+}$

**Effect of pH.** The adsorption of Ba$^{2+}$ ions by MIL-101-SO$_3$H is strongly influenced by pH due to changes in the surface charge of the adsorbent. In acidic conditions, specifically around pH = 4, the sulfonated groups (–SO$_3$H) on MIL-101-SO$_3$H undergo partial deprotonation, leading to a negatively charged surface. This negative charge enhances the electrostatic attraction between the MIL-101-SO$_3$H surface and the positively charged Ba$^{2+}$ ions, resulting in higher adsorption efficiency. At basic pH levels, however, the protonation extent increases, and competing hydroxide ions (OH$^-$) in the solution may also affect Ba$^{2+}$ binding. Moreover, higher pH values more than 11 may lead to the precipitation of Ba$^{2+}$, resulting in making a mistake in adsorption measurement. These factors make acidic pH conditions, particularly around pH = 4, optimal for Ba$^{2+}$ adsorption, as shown in Fig. 6a. To highlight the effect of –SO$_3$H in adsorption process, the adsorption behavior of MIL-101 is also assessed. Consequently, a pH of 4 was selected for further experiments to maximize the adsorptive performance of MIL-101-SO$_3$H.

**Effect of initial concentration of Ba$^{2+}$.** The initial concentration of Ba$^{2+}$ significantly affects the adsorption efficiency of MIL-101-SO$_3$H. At lower initial concentrations, such as 50 and 100 ppm, the adsorption efficiency reaches as high as 99.4% and 94.65%, respectively, indicating that the available adsorption sites on the MOF are sufficient to capture nearly all Ba$^{2+}$

| Material | Zeta Potential |
|---|---|
| MIL-101 | -14.98 mV |
| MIL-101-SO$_3$H | 1.31 mV |



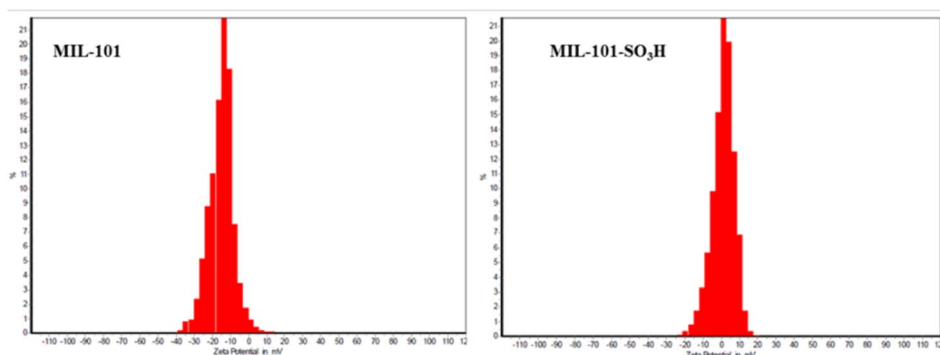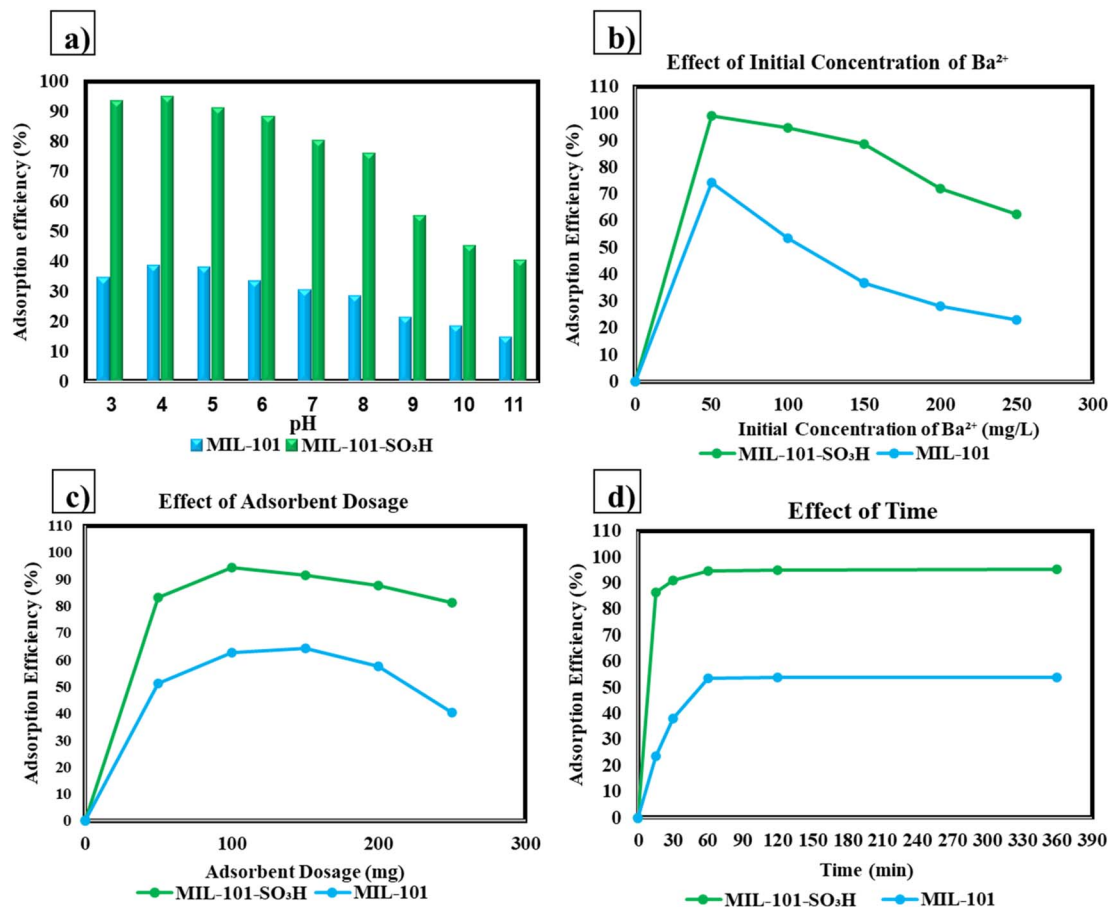**Fig. 5** The zeta potential of MIL-101 (left) and MIL-101-SO$_3$H (right).

**Fig. 6** Effect of pH (a), effect of initial concentration of Ba$^{2+}$ (b), effect of adsorbent dosage (c) and effect of contact time (d) on adsorption behavior of MIL-101 and MIL-101-SO$_3$H toward Ba$^{2+}$.

ions present (Fig. 6b). However, as the concentration of Ba$^{2+}$ increases (150 to 250 ppm), the adsorption efficiency gradually decreases to 62.3%. This reduction is attributed to the saturation of active sites on MIL-101-SO$_3$H; as the concentration increases, fewer binding sites are available, and consequently, the MOF's capacity to adsorb further Ba$^{2+}$ ions decline. The role of –SO$_3$H groups in enhancing Ba$^{2+}$ adsorption becomes evident when comparing the adsorption efficiencies of MIL-101-SO$_3$H with that of MIL-101 without –SO$_3$H groups. At corresponding concentrations of Ba$^{2+}$ (50 to 250 ppm), the adsorption efficiencies for MIL-101 are 74.4%, 53.5%, 36.8%, 28.2%, and 20.2%, respectively, demonstrating significantly lower performance than MIL-101-SO$_3$H. This contrast highlights the strong interaction between the –SO$_3$H functional groups and Ba$^{2+}$ ions, suggesting that the –SO$_3$H groups enhance the affinity of MIL-101-SO$_3$H for Ba$^{2+}$ and improve its overall adsorption efficiency, especially at lower concentrations. Therefore, the sulfonated MOF shows a much higher potential for effective Ba$^{2+}$ removal, especially when dealing with lower contaminant levels. Fig. 6c and d illustrates the trend of adsorption for both MOFs.

**Effect of adsorbent dosage.** The adsorbent dosage of MIL-101-SO$_3$H has a notable impact on the adsorption efficiency for Ba$^{2+}$ ions. At lower dosages, such as 10 mg, the adsorption efficiency reaches 83.2%, which increases as the dosage rises,

peaking at 99.4% with a dosage of 30 mg. This increase in efficiency with higher dosages is likely due to the greater availability of active sites for Ba$^{2+}$ ions. However, when the dosage is further increased to 40 and 50 mg, a decrease in adsorption efficiency is observed, dropping to 90.65% and 84.2%, respectively. This reduction at higher dosages can be attributed to the agglomeration of MIL-101-SO$_3$H particles, which can block some active sites and reduce the accessibility for Ba$^{2+}$ ions, thus limiting further adsorption. To emphasize the role of the –SO$_3$H functional group in Ba$^{2+}$ adsorption, we compared the efficiency of MIL-101-SO$_3$H with MIL-101 without the –SO$_3$H group. At the same dosages (10 to 50 mg), MIL-101 shows lower adsorption efficiencies of 51.2%, 62.8%, 74.4%, 57.5%, and 40.3%, respectively. This comparison indicates that the –SO$_3$H group enhances the adsorption capacity of MIL-101-SO$_3$H for Ba$^{2+}$, especially at lower dosages, by increasing the affinity between the adsorbent and Ba$^{2+}$ ions. Therefore, the sulfonated MIL-101-SO$_3$H shows superior adsorption behavior over the non-functionalized MIL-101, particularly at optimized dosages. Fig. 6c shows the trend of adsorption efficiency in various dosage of the both adsorbents.

**Effect of contact time.** The effect of contact time on Ba$^{2+}$ adsorption by MIL-101-SO$_3$H indicates that adsorption efficiency rises rapidly in the initial stages and then gradually

reaches equilibrium. As demonstrated in Fig. 6d, at 15 minutes, the adsorption efficiency is 86.6%, which increases to 91.2% at 30 minutes and 94.65% at 60 minutes. A slower increase follows, reaching 95.2% at 120 minutes, which remains nearly constant after 120 minutes. This stabilization suggests that equilibrium is achieved after approximately 120 minutes, where most of the active sites on MIL-101-SO$_3$H are occupied by Ba$^{2+}$ ions, and further increase in contact time does not significantly improve adsorption. For comparison, the adsorption efficiency of non-sulfonated MIL-101 is considerably lower, with values of 23.5%, 38.2%, 53.5%, 53.8%, and 53.88% at 15, 30, 60, 120, and 360 minutes, respectively. This highlights the substantial impact of the –SO$_3$H functional groups on MIL-101, which enhance the adsorption efficiency by creating additional active sites that favor Ba$^{2+}$ adsorption. The –SO$_3$H groups allow for a faster approach to equilibrium and significantly higher adsorption capacities in a shorter time frame compared to non-functionalized MIL-101. Therefore, the functionalization of MIL-101 with –SO$_3$H groups enhances both the efficiency and rate of Ba$^{2+}$ ion adsorption.

**Adsorption isotherms.** The adsorption isotherm analysis for Ba$^{2+}$ ions on MIL-101-SO$_3$H indicates that the Langmuir model better describes the adsorption process compared to the Freundlich model, as evidenced by the correlation coefficients of 0.9931 for Langmuir and 0.9194 for Freundlich (Fig. 7). The high correlation coefficient for the Langmuir model suggests that Ba$^{2+}$ adsorption onto MIL-101-SO$_3$H primarily follows monolayer adsorption on a homogeneous surface with uniform active sites. In the Langmuir model, it is assumed that once a Ba$^{2+}$ ion occupies an adsorption site, no further adsorption can occur at that site, indicating limited active sites and a maximum adsorption capacity. In contrast, the Freundlich model, with its lower correlation coefficient, describes adsorption on a heterogeneous surface, with varying affinities across different sites. The less fitting Freundlich model in this case suggests that surface heterogeneity plays a less significant role, and the adsorbent's active sites have a relatively uniform affinity for Ba$^{2+}$ ions. Therefore, the adsorption is primarily governed by uniform interactions between Ba$^{2+}$ ions and the –SO$_3$H functional groups in the MOF structure, making the Langmuir model a more accurate representation of this adsorption process. This insight helps in understanding the adsorption mechanism and confirms the suitability of MIL-101-SO$_3$H as an

efficient adsorbent for Ba$^{2+}$ ions in a controlled and predictable manner.

**Optimized adsorption conditions and capacity comparison.** Based on the experiments, the best adsorption conditions for barium ions were established by changing the amount of barium ions and the amount of adsorbent. Equilibrium was achieved at initial 150 mg g$^{-1}$ of barium ions and 100 mg of adsorbent. At this condition the maximum adsorption capacity of Ba$^{2+}$ by MIL-101-SO$_3$H was estimated to be 141.9 mg g$^{-1}$ while the unmodified MIL-101 had an adsorption capacity of 54 mg g$^{-1}$. This shows that the performance of MIL-101-SO$_3$H is better than the parent material due to sulfonation which may lead to increase in surface area and more functional groups that can interact with barium ions. The outcomes presented in this paper are important in order to understand how to use MIL-101-SO$_3$H effectively as an adsorbent for the removal of barium in the environment.

Table 1 compares the adsorption capacities of various materials towards Ba$^{2+}$ ions, demonstrating the exceptional performance of MIL-101-SO$_3$H. Adsorption capacities vary widely, from the low capacity of activated carbon ($3.1 \times 10^{-6}$ mg g$^{-1}$) to the impressive 295.52 mg g$^{-1}$ for Ti$_3$C$_2$T$_x$ MXene. MIL-101-SO$_3$H stands out with a capacity of 141.9 mg g$^{-1}$, significantly surpassing materials like titanium nanotubes (109.6 mg g$^{-1}$) and the unmodified MIL-101 (54.0 mg g$^{-1}$). This enhanced performance is attributed to the functionalized –SO$_3$H groups on MIL-101-SO$_3$H, which introduce additional active sites for barium ion adsorption, resulting in improved efficiency. Notably, MIL-101-SO$_3$H outperforms materials such as expanded perlite (2.486 mg g$^{-1}$) and zero-valent iron (22.56 mg g$^{-1}$), highlighting its potential for environmental applications like water treatment. Although certain materials, such as Ti$_3$C$_2$T$_x$ MXene (295.52 mg g$^{-1}$) and [CH$_3$CH$_2$NH$_3$]$_3$In$_2$S$_5$ (211.73 mg g$^{-1}$), exhibit higher adsorption capacities, MIL-101-SO$_3$H offers a competitive performance while maintaining structural stability, ease of synthesis, and cost-effectiveness. These factors make MIL-101-SO$_3$H a highly promising candidate for large-scale, cost-effective Ba$^{2+}$ removal in industrial and environmental applications.

Previous studies have reported an adsorption capacity of 70.5 mg g$^{-1}$ for MIL-101-SO$_3$H when the sulfonated functional group was located on the ligand.[1] In contrast, our results show a significantly higher adsorption capacity of 141.9 mg g$^{-1}$ when
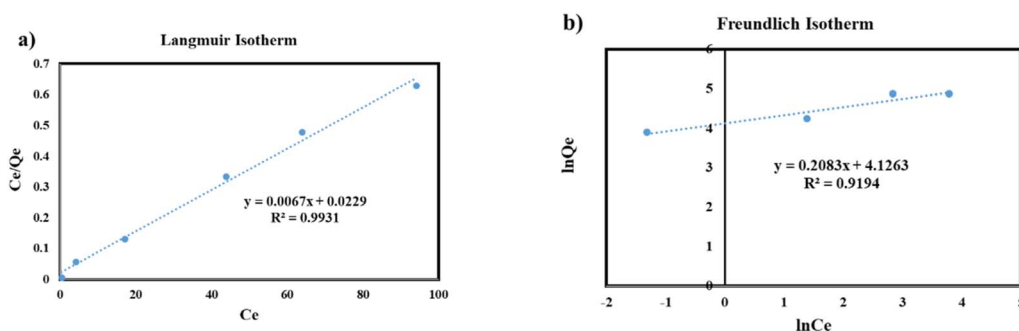


**Fig. 7** Langmuir (a) and Freundlich (b) isotherms of barium adsorption over MIL–101–SO$_3$H.

**Table 1** Comparison of adsorption capacities of various materials for $Ba^{2+}$ ions. Adsorption capacities are expressed in mg of $Ba^{2+}$ per gram of adsorbent

| No. | Material | Adsorption capacity | Ref. |
|---|---|---|---|
| 1 | Activated carbon | $3.1 \times 10^{-6}$ mg g$^{-1}$ | 42 |
| 2 | Titanate nanotube | 109.6 mg g$^{-1}$ | 43 |
| 3 | MOF-808-SO$_4$ | 131.1 mg g$^{-1}$ | 1 |
| 4 | Expanded perlite | 2.486 mg g$^{-1}$ | 44 |
| 5 | Zero-valent iron | 22.56 mg g$^{-1}$ | 45 |
| 6 | Niobate | 13.7 mg g$^{-1}$ | 46 |
| 7 | Ca-exchanged clinoptilolite | 71.885 mg g$^{-1}$ | 47 |
| 8 | Titanium silicate | 144 mg g$^{-1}$ | 48 |
| 9 | $[CH_3CH_2NH_3]_6In_8S_{15}$ | 211.73 mg g$^{-1}$ | 49 |
| 10 | TiY$_2$O$_5$@g-C$_3$N$_4$ | 295.52 mg g$^{-1}$ | 50 |
| 11 | $K_{3.4}(CH_3NH_3)_{0.45}(NH_4)_{0.15}Zn_2Sn_3Se_{10}\cdot3.4H_2O$ | 108.94 mg g$^{-1}$ | 51 |
| 12 | Ti$_3$C$_2$T$_x$ MXene | 180 mg g$^{-1}$ | 52 |
| 13 | **MIL-101(Cr)** | **54.0 mg g$^{-1}$** | **This work** |
| 14 | **MIL-101-SO$_3$H** | **141.9 mg g$^{-1}$** | **This work** |

the sulfonation is introduced at the metal center of MIL-101. This enhancement in adsorption capacity can be attributed to several factors. First, the sulfonation of the metal center increases the number of accessible active sites for barium ion binding, improving the overall adsorption efficiency. The sulfonic acid groups at the metal centers likely interact more strongly with $Ba^{2+}$ ions due to electrostatic and coordination interactions, leading to higher binding strength compared to the sulfonation at the ligand. Additionally, the proximity of the functional group to the metal center enhances the structural integrity and stability of the framework, preventing leaching of the functional groups during adsorption. These combined effects contribute to the superior adsorption performance of MIL-101-SO$_3$H when the sulfonation is positioned on the metal center.

**Selectivity test.** The evaluation of adsorption efficiency in the presence of coexisting species is critical to understand the practical applicability of MIL-101-SO$_3$H in real-world scenarios. In our study, Cs, Ni, Cr, and Zn were introduced as coexisting ions to assess the selectivity and adsorption capacity of the adsorbent toward $Ba^{2+}$ ions. As illustrated in Fig. 8, MIL-101-SO$_3$H demonstrated high adsorption efficiencies for $Ba^{2+}$ at the presence of coexisting ions, highlighting its superior affinity

and capacity for cation adsorption. This finding underscores the robust performance of MIL-101-SO$_3$H in complex aqueous solutions where multiple competing ions are present, as is often the case in environmental and industrial wastewater. The results emphasize the importance of the sulfonic acid (–SO$_3$H) functional groups, which likely enhance the selectivity and interaction strength with cations through electrostatic attractions and coordination mechanisms. This ability to effectively remove target ions, even in the presence of competing species, positions MIL-101-SO$_3$H, as a promising material for the remediation of multi-contaminant systems, ensuring efficient and selective pollutant removal in diverse applications.

**Desorption test.** The desorption efficiency of cations from a MOF after immersion in water depends on the interplay between the MOF's adsorption characteristics and the concentration gradient driving the desorption process. Desorption occurs when the cations detach from the MOF surface and move into the surrounding water. The efficiency of this process depends on the concentration gradient between the MOF and the water. If the initial concentration of the analyte in water is low, the concentration gradient is high, promoting effective desorption. However, as the initial analyte concentration increases, this gradient diminishes, reducing the driving force for desorption. High initial analyte concentrations in water may reduce the chemical potential difference between the MOF and the solution. This could result in a lower desorption efficiency because the system approaches equilibrium, where less mass transfer occurs. It should be noticed that at higher initial concentrations of the analyte, adsorption sites on the MOF may become more saturated. Saturation reduces the binding strength of additional cations, which could, paradoxically, make desorption easier since the cations are held less strongly. Table 2 shows the desorption efficiency of both MOFs after 2 h of immersing in fresh water. The results highlight the importance of –SO$_3$H role in the adsorption–desorption process.

The high desorption efficiency of $Ba^{2+}$ in water (75.4–89.6%, Table 2) arises from: competitive ion exchange and concentration-driven diffusion.
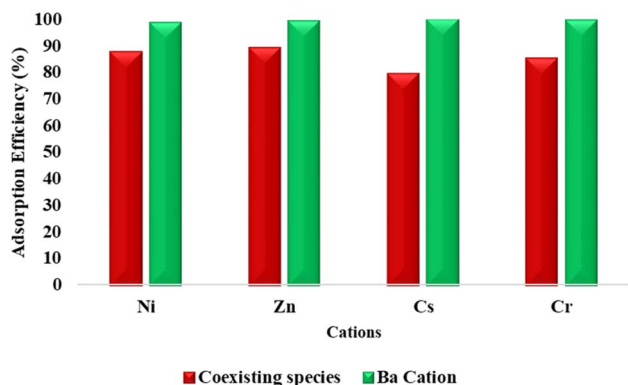


**Fig. 8** Adsorption of barium in the presence of other cations.

**Table 2**  Desorption of $Ba^{2+}$ from MIL-101 and MIL-101-$SO_3H$

| Desorption efficiency of $Ba^{2+}$ after 2 hours | | |
|---|---|---|
| Initial concentration | MIL-101 | MIL-101-$SO_3H$ |
| 50 ppm | 28.7% | 75.4% |
| 100 ppm | 22.7% | 81.2% |
| 150 ppm | 14.7% | 89.6% |

(1) Competitive ion exchange: water's weak acidity (pH ~7) provides $H^+$ ions that displace $Ba^{2+}$ from sulfonate sites ($-SO_3^-$) *via* reversible ion exchange (Fig. 10). This is consistent with studies on sulfonated MOFs, where $H^+/Ba^{2+}$ competition governs regeneration efficiency.[1]

(2) Concentration-driven diffusion: at low $Ba^{2+}$ concentrations (50 ppm), the steep chemical potential gradient between the MOF and water maximizes desorption. At higher concentrations (150 ppm), site saturation weakens $Ba^{2+}$ binding, enhancing release despite a reduced gradient.[14,53]

While acidic eluents (*e.g.*, 0.1 M HCl) could fully regenerate –$SO_3H$ groups,[33] water offers a greener alternative that preserves MIL-101-$SO_3H$'s crystallinity (XRD, Fig. 9a) and porosity (BET, Fig. 11), critical for reuse.[54]

**Effect of $Ba^{2+}$ absorption on the MOFs structure.** The XRD patterns of MIL-101 and MIL-101-$SO_3H$, both before and after $Ba^{2+}$ adsorption, reveal the effects of $Ba^{2+}$ on the structural integrity of the frameworks. For pristine MIL-101 and MIL-101-$SO_3H$, sharp diffraction peaks are observed, characteristic of their highly crystalline structure. These peaks are consistent with the well-defined framework of MIL-101 and its sulfonated derivative (MIL-101-$SO_3H$). After the adsorption of $Ba^{2+}$, noticeable changes occur in the XRD patterns. In MIL-101, the peak intensities slightly decrease, indicating partial distortion or reduction in crystallinity due to interactions between $Ba^{2+}$ ions and the framework. However, the overall pattern remains intact, suggesting that the structural stability of MIL-101 is

largely preserved during the adsorption process. In MIL-101-$SO_3H$, the changes are more pronounced. A shift in peak positions and further reduction in intensity are observed. These modifications suggest stronger interactions between the $Ba^{2+}$ ions and the –$SO_3H$ functional groups, potentially causing slight framework strain or distortion. The sulfonic acid groups likely enhance the binding of $Ba^{2+}$, leading to more significant structural changes compared to pristine MIL-101. Despite these modifications, the presence of discernible peaks in both materials after adsorption indicates that the frameworks remain largely stable and maintain their adsorption capabilities. These results, which are observable in Fig. 9a, highlight the robust nature of MIL-101 and MIL-101-$SO_3H$, as well as the enhanced affinity of the sulfonated material for $Ba^{2+}$ ions, making it more effective in adsorption applications.

Furthermore, as illustrated in Fig. 9b, the FT-IR spectra show significant insights into the $Ba^{2+}$ adsorption effect on both MIL-101 and MIL-101-$SO_3H$. For MIL-101-$SO_3H$, the presence of sulfonic acid (–$SO_3H$) functional groups is confirmed by the characteristic peaks near 1040–1150 $cm^{-1}$, corresponding to S–O and O=S=O vibrations. After $Ba^{2+}$ adsorption, these peaks exhibit a slight broadening, suggesting strong interaction between the $Ba^{2+}$ cations and the –$SO_3H$ groups. This interaction likely involves ion exchange or electrostatic attraction. In MIL-101 without –$SO_3H$ functionalization, the absence of such pronounced shifts in the FT-IR spectrum indicates weaker or less specific adsorption of $Ba^{2+}$, aligning with its lower adsorption efficiency. Additionally, any changes in the broader O–H stretching region (~3200–3600 $cm^{-1}$) suggest a role of hydroxyl groups in binding $Ba^{2+}$ ions. Overall, the sulfonic acid functionalization in MIL-101-$SO_3H$ enhances $Ba^{2+}$ interaction, as evident from the spectral changes.

**DLS and zeta potential.** The adsorption of barium ions has a significant impact on the surface charge of both MIL-101 and MIL-101-$SO_3H$, as indicated by the changes in their zeta potential values (Fig. 10). For MIL-101, the zeta potential remains at −9.60 mV after barium adsorption, which suggests
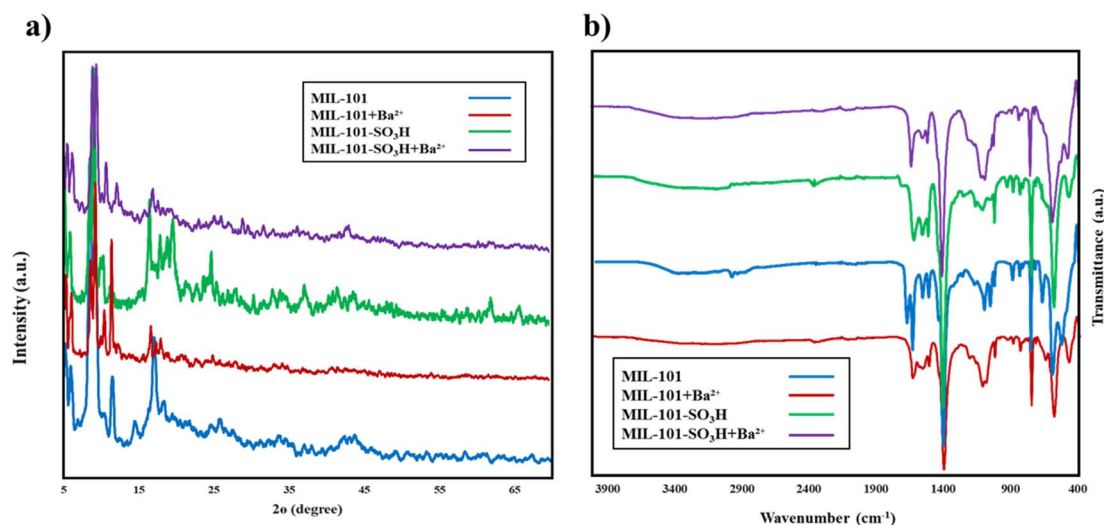


**Fig. 9**  XRD patterns (a) and FT-IR spectra (b) of both MIL-101 and MIL-101-$SO_3H$ before and after adsorption of $Ba^{2+}$.

© 2025 The Author(s). Published by the Royal Society of Chemistry

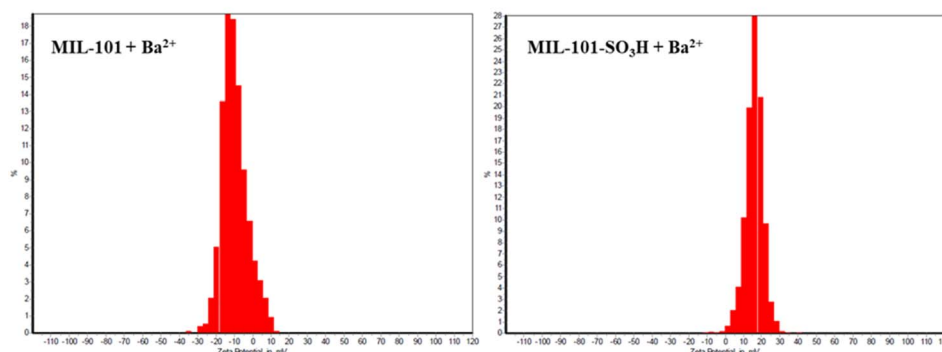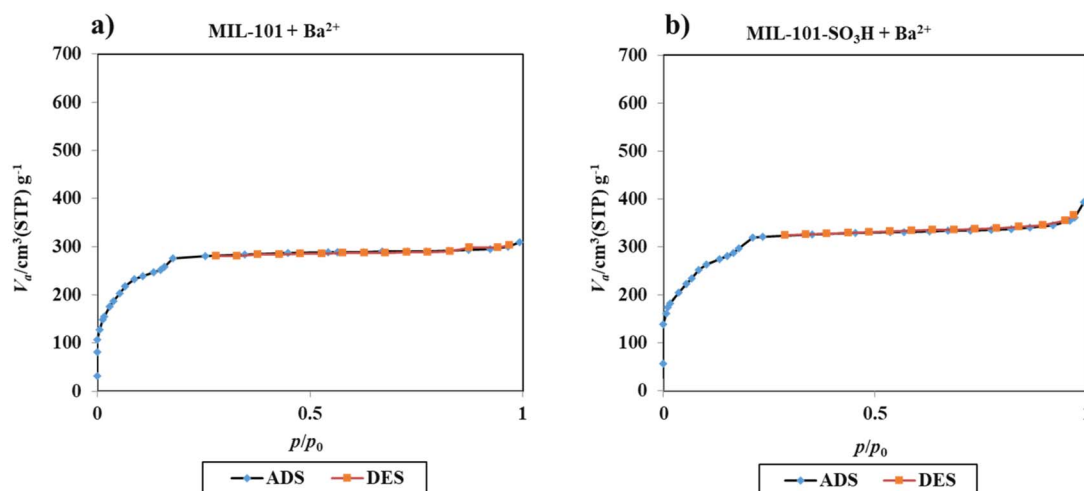| Material | Zeta Potential |
|---|---|
| MIL-101 + Ba$^{2+}$ | -9.60 mV |
| MIL-101-SO$_3$H + Ba$^{2+}$ | 16.13 mV |



**Fig. 10** Zeta potential of MIL-101 (left) and MIL-101-SO$_3$H (right) after barium adsorption.

that the barium ions interact with the carboxylate groups (–COO$^-$) within the framework, or that the adsorption process does not greatly alter the overall surface charge of the material. In contrast, the zeta potential of MIL-101-SO$_3$H shifts significantly to +16.13 mV after barium adsorption. This positive shift can be attributed to the strong electrostatic interaction between Ba$^{2+}$ ions and the sulfonate functional groups (–SO$_3$H) on the MOF surface. The adsorption of Ba$^{2+}$ ions neutralize



| | MIL-101 + Ba$^{2+}$ | MIL-101-SO$_3$H + Ba$^{2+}$ |
|---|---|---|
| **V$_m$** | 194.28 [cm$^3$(STP) g$^{-1}$] | 251.87 [cm$^3$(STP) g$^{-1}$] |
| **a$_{s,BET}$** | 845.61 [m$^2$ g$^{-1}$] | 1096.3 [m$^2$ g$^{-1}$] |
| **C** | 269.8 | 110.17 |
| **Total pore volume(p/p$_0$=0.990)** | 0.4776 [cm$^3$ g$^{-1}$] | 0.6026 [cm$^3$ g$^{-1}$] |
| **Average pore diameter** | 2.2593 [nm] | 2.1987 [nm] |

**Fig. 11** N$_2$ adsorption–desorption of MIL-101 (a) and MIL-101-SO$_3$H (b) after barium adsorption.

some of the negative charges from the sulfonate groups, leading to an overall increase in positive surface charge. This substantial change in zeta potential indicates that the sulfonation of MIL-101 at the metal center enhances the material's affinity for barium ions through electrostatic attraction and coordination interactions. These findings underscore the role of $-SO_3H$ functional groups in modulating the adsorption behavior and surface charge dynamics of MIL-101-$SO_3H$, making it a highly effective material for barium ion removal.

**BET analysis.** The structural properties of MIL-101 and MIL-101-$SO_3H$, both before and after barium adsorption, reveal important insights based on BET surface area, pore volume, and pore size data (Fig. 11). Before barium adsorption, MIL-101 exhibits a higher BET surface area (2055.4 $m^2$ $g^{-1}$) and pore volume (0.9614 $cm^3$ $g^{-1}$) compared to MIL-101-$SO_3H$, which has a surface area of 1302.8 $m^2$ $g^{-1}$ and a pore volume of 0.7617 $cm^3$ $g^{-1}$. This difference is due to the presence of sulfonate functional groups in MIL-101-$SO_3H$ that partially occupy the mesopores. However, after barium adsorption, both materials show a notable reduction in surface area and pore volume, with MIL-101-$SO_3H$ retaining higher values (1096.3 $m^2$ $g^{-1}$, 0.6026 $cm^3$ $g^{-1}$) compared to MIL-101 (845.61 $m^2$ $g^{-1}$, 0.4776 $cm^3$ $g^{-1}$). This indicates that MIL-101-$SO_3H$ can effectively accommodate barium ions while maintaining its structural stability. Additionally, the pore diameter of MIL-101-$SO_3H$ slightly decreases from 2.3386 nm to 2.1987 nm, indicating effective ion

confinement, whereas MIL-101 shows a slight increase from 1.871 nm to 2.2593 nm, potentially due to structural rearrangements during adsorption. The $C$-values further highlight the adsorption dynamics, with a significant decrease for MIL-101-$SO_3H$ (+$Ba^{2+}$), indicating uniform adsorption behavior, while a sharp increase for MIL-101 (+$Ba^{2+}$) suggests greater surface heterogeneity. These results demonstrate that the sulfonate functional groups in MIL-101-$SO_3H$ enhance barium adsorption efficiency and selectivity, making it a superior adsorbent compared to its unmodified counterpart.

**XPS analysis.** The XPS spectra of all structures show several characteristic peaks, which are important for understanding the elemental composition and chemical environment of them, as can be seen in Fig. 12. In the case of pristine MIL-101, the peaks at around 285 eV and 530 eV are often attributed to the presence of carbon (C 1s) and oxygen (O 1s), respectively. The carbon peak likely originates from the organic linkers in the MIL-101 framework, while the oxygen peak is associated with both the organic linkers and metal–oxygen bonds within the structure. A significant peak around 710–730 eV typically corresponds to chromium (Cr 2p), which is characteristic of the chromium in the MIL-101 structure. The exact position of the Fe 2p peak can provide insight into the oxidation state of Cr. In the high-intensity regions, the large peak observed near 600 eV could be related to Auger peaks or other transition effects in the spectrum. The intensity suggests a strong presence of elements
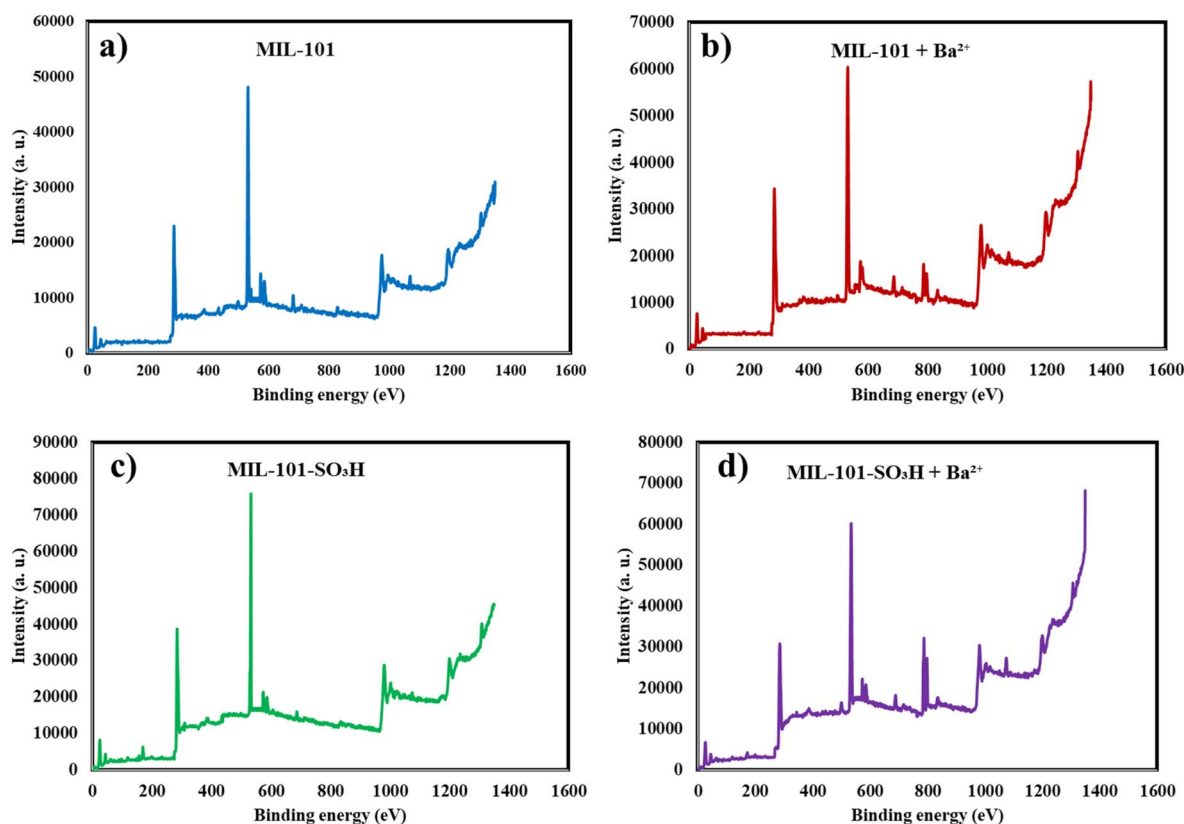


Fig. 12 XPS spectra of pristine MIL-101 (a), MIL-101 after $Ba^{2+}$ adsorption (b), pristine MIL-101-$SO_3H$ (c), and MIL-101-$SO_3H$ after $Ba^{2+}$ adsorption (d).

with core-level transitions in this binding energy range. Broad peaks at high binding energy above 1200 eV might be associated with background noise or detector sensitivity issues, which sometimes appear in XPS spectra.

The XPS spectrum of MIL-101 after adsorption of $Ba^{2+}$ shows some noticeable changes compared to the pristine MIL-101 sample. The overall intensity of the peaks has increased, particularly the primary peaks around 400 eV, 600 eV, and 1200 eV, which suggests an alteration in the electronic environment of the material. After $Ba^{2+}$ adsorption, new peaks corresponding to Ba 3d may appear around the 780–800 eV region, which indicates successful adsorption of $Ba^{2+}$ ions onto the MIL-101 structure. This shift reflects the binding interaction between $Ba^{2+}$ ions and the functional groups present in MIL-101. Moreover, peaks related to the oxygen species (often around 531 eV for O 1s) and carbonyl groups (around 285 eV for C 1s) may exhibit shifts or intensity changes. This is due to the interaction of $Ba^{2+}$ with oxygen-containing groups, which enhances binding affinity. The increase in electron counts across various peaks suggests that $Ba^{2+}$ adsorption may have introduced additional electronic density, consistent with the coordination of $Ba^{2+}$ with the oxygen or sulfonate.

The XPS analysis of pristine MIL-101-$SO_3H$ also shows a peak at C 1s region (approx. ~285 eV). Deconvolution of this peak could show components related to aromatic carbon, oxygen-bonded carbon, and possibly sulfur-containing groups. The peak at O 1s region (~532 eV) represents oxygen contributions from hydroxyl groups, sulfonic acid groups (–$SO_3H$), and the carboxyl groups in the framework structure. S 2p region (~168–170 eV) confirms the presence of sulfonic acid groups (–$SO_3H$) in the modified MIL-101. The binding energy aligns with the sulfur atom in a highly oxidized state (as in $SO_3$).

The XPS spectrum of MIL-101-$SO_3H$ after $Ba^{2+}$ adsorption shows several significant features when compared to its pristine counterpart. The characteristic binding energy for the sulfur atoms in the –$SO_3H$ groups may experience a slight shift or intensity variation. This indicates interactions between the –$SO_3H$ groups and the adsorbed $Ba^{2+}$ ions, likely through ion-exchange mechanisms or electrostatic attraction. A clear indication of $Ba^{2+}$ adsorption is the appearance of new peaks in the Ba 3d region (around 780–795 eV), representing the presence of barium on the material's surface. The oxygen (O 1s) and sulfur (S 2p) peaks may shift slightly due to changes in the electronic environment after interaction with $Ba^{2+}$. This highlights the role of –$SO_3H$ functional groups in binding barium ions. Moreover, peaks corresponding to framework metals (e.g., Cr in MIL-101) might exhibit minor changes in intensity or broadening. This could result from structural rearrangements or surface modifications following $Ba^{2+}$ adsorption.

## Conclusion

Current study demonstrates that sulfonic acid functionalization at the metal centers of MIL-101(Cr) significantly enhances its barium ion adsorption capacity (141.9 mg g$^{-1}$) compared to the unmodified framework (54 mg g$^{-1}$). The optimized MIL-101-$SO_3H$ exhibits excellent removal efficiency (99% at pH = 4), with

adsorption following the Langmuir isotherm model. Characterization studies confirm that the sulfonation strategy preserves the MOF's structural integrity while introducing effective binding sites for $Ba^{2+}$. Looking forward, this work suggests three key directions for further development: investigation of long-term stability and reusability under various environmental conditions, molecular-level studies of binding mechanisms through computational modeling, and scale-up trials to evaluate practical wastewater treatment applications. These future studies would build upon the fundamental insights gained here while addressing important considerations for real-world implementation. The metal-center functionalization approach presented here offers a promising strategy for designing MOF-based adsorbents tailored for heavy metal removal, with potential extensions to other environmentally relevant contaminants.

## Data availability

Relevant data supporting the key findings of this study are available within the article.

## Conflicts of interest

The authors declare no competing interests.

## Acknowledgements

## References

1 Y. Peng, H. Huang, D. Liu and C. Zhong, *ACS Appl. Mater. Interfaces*, 2016, **8**, 8527–8535.
2 H. A. Aziz, M. F. Ghazali, Y.-T. Hung and L. K. Wang, in *Handbook of Advanced Industrial and Hazardous Wastes Management*, CRC Press, 2017, pp. 463–482.
3 J. Kravchenko, T. H. Darrah, R. K. Miller, H. K. Lyerly and A. Vengosh, *Environ. Geochem. Health*, 2014, **36**, 797–814.
4 A. K. Fard, G. McKay, R. Chamoun, T. Rhadfi, H. Preud'Homme and M. A. Atieh, *Chem. Eng. J.*, 2017, **317**, 331–342.
5 Z. Majidnia, A. Idris, M. Majid, R. Zin and M. Ponraj, *Appl. Radiat. Isot.*, 2015, **105**, 105–113.
6 M. R. Abukhadra, S. M. Ali, A. M. El-Sherbeeny, A. T. A. Soliman and A. E. E. Abd Elgawad, *Inorg. Chem. Commun.*, 2020, **119**, 108053.
7 X. Zhang, Z. Chen, X. Liu, S. L. Hanna, X. Wang, R. Taheri-Ledari, A. Maleki, P. Li and O. K. Farha, *Chem. Soc. Rev.*, 2020, **49**, 7406–7427.
8 J.-P. Zhang, H.-L. Zhou, D.-D. Zhou, P.-Q. Liao and X.-M. Chen, *Natl. Sci. Rev.*, 2018, **5**, 907–919.
9 S. Ma and H.-C. Zhou, *Chem. Commun.*, 2010, **46**, 44–53.
10 X. Zhao, Y. Wang, D. S. Li, X. Bu and P. Feng, *Adv. Mater.*, 2018, **30**, 1705189.

11 M. Ranocchiari and J. A. van Bokhoven, *Phys. Chem. Chem. Phys.*, 2011, **13**, 6388–6396.

12 P. Kumar, V. Bansal, K.-H. Kim and E. E. Kwon, *J. Ind. Eng. Chem.*, 2018, **62**, 130–145.

13 S. D. Taherzade, M. Abbasichaleshtori and J. Soleimannejad, *RSC Adv.*, 2022, **12**, 9023–9035.

14 X. Zhao, L. Pei, Y.-N. Zhang, H. Huang, X. Zheng, B. Liu and M. Tong, *Green Chem. Eng.*, 2022, **3**, 405–412.

15 P. Liu, P. Yang, J. Yang and J. Gu, *Chem. Commun.*, 2021, **57**, 5822–5825.

16 H. Belarbi, L. Boudjema, C. Shepherd, N. Ramsahye, G. Toquer, J.-S. Chang and P. Trens, *Colloids Surf., A*, 2017, **520**, 46–52.

17 H. Zhang, X. Hu, T. Li, Y. Zhang, H. Xu, Y. Sun, X. Gu, C. Gu, J. Luo and B. Gao, *J. Hazard. Mater.*, 2022, **429**, 128271.

18 T. Loiseau, C. Serre, C. Huguenard, G. Fink, F. Taulelle, M. Henry, T. Bataille and G. Férey, *Chem. - Eur. J.*, 2004, **10**, 1373–1382.

19 M. Ma, H. Noei, B. Mienert, J. Niesel, E. Bill, M. Muhler, R. A. Fischer, Y. Wang, U. Schatzschneider and N. Metzler-Nolte, *Chem. - Eur. J.*, 2013, **19**, 6785–6790.

20 S. Bhattacharjee, C. Chen and W.-S. Ahn, *RSC Adv.*, 2014, **4**, 52500–52525.

21 Z. Zhang, S. Huang, S. Xian, H. Xi and Z. Li, *Energy Fuels*, 2011, **25**, 835–842.

22 M. Y. Zorainy, M. G. Alalm, S. Kaliaguine and D. C. Boffito, *J. Mater. Chem. A*, 2021, **9**, 22159–22217.

23 Z. Li, X. Liu, W. Jin, Q. Hu and Y. Zhao, *J. Colloid Interface Sci.*, 2019, **554**, 692–704.

24 M. Zou, M. Dong and T. Zhao, *Int. J. Mol. Sci.*, 2022, **23**, 9396.

25 M. Shafiei, M. S. Alivand, A. Rashidi, A. Samimi and D. Mohebbi-Kalhori, *Chem. Eng. J.*, 2018, **341**, 164–174.

26 L. Bromberg, Y. Diao, H. Wu, S. A. Speakman and T. A. Hatton, *Chem. Mater.*, 2012, **24**, 1664–1675.

27 S. Kayal, B. Sun and A. Chakraborty, *Energy*, 2015, **91**, 772–781.

28 J. Chen, X. Chen, Z. Zhang, Z. Bao, H. Xing, Q. Yang and Q. Ren, *Mol. Catal.*, 2018, **445**, 163–169.

29 M.-L. Chen, S.-Y. Zhou, Z. Xu, L. Ding and Y.-H. Cheng, *Molecules*, 2019, **24**, 3718.

30 A. E. Khudozhitkov, S. S. Arzumanov, D. I. Kolokolov, O. A. Kholdeeva, D. Freude and A. G. Stepanov, *Chem. - Eur. J.*, 2019, **25**, 5163–5168.

31 B. Tan, Y. Luo, X. Liang, S. Wang, X. Gao, Z. Zhang and Y. Fang, *Ind. Eng. Chem. Res.*, 2019, **58**, 2983–2990.

32 Y. Jin, J. Shi, F. Zhang, Y. Zhong and W. Zhu, *J. Mol. Catal. A: Chem.*, 2014, **383**, 167–171.

33 Z. Hasan, J. W. Jun and S. H. Jhung, *Chem. Eng. J.*, 2015, **278**, 265–271.

34 J. Hou, F. AlGhunaimi, T. P. Huang and N. Aljuryyed, 2024.

35 Y. Peng, H. Huang, D. Liu and C. Zhong, *ACS Appl. Mater. Interfaces*, 2016, **8**, 8527–8535.

36 G. Férey, C. Mellot-Draznieks, C. Serre, F. Millange, J. Dutour, S. Surblé and I. Margiolaki, *Science*, 2005, **309**, 2040–2042.

37 S. S. Mortazavi, A. Abbasi, M. Masteri-Farahani and F. Farzaneh, *ChemistrySelect*, 2019, **4**, 7495–7501.

38 Z. Li, S. Zhao, H. Wang, Y. Peng, Z. Tan and B. Tang, *Colloids Surf., B*, 2019, **178**, 1–7.

39 H. Deng, C. J. Doonan, H. Furukawa, R. B. Ferreira, J. Towne, C. B. Knobler, B. Wang and O. M. Yaghi, *science*, 2010, **327**, 846–850.

40 B. Smith, 2016.

41 Y. Pan, B. Yuan, Y. Li and D. He, *Chem. Commun.*, 2010, **46**, 2280–2282.

42 H. Gad, Y. Lasheen and T. El-Zakla, *Radiochemistry*, 2013, **55**, 589–595.

43 M. Xu, G. Wei, N. Liu, L. Zhou, C. Fu, M. Chubik, A. Gromov and W. Han, *Nanoscale*, 2014, **6**, 722–725.

44 M. Torab-Mostaedi, A. Ghaemi, H. Ghassabzadeh and M. Ghannadi-Maragheh, *Can. J. Chem. Eng.*, 2011, **89**, 1247–1254.

45 O. Celebi, Ç. Üzüm, T. Shahwan and H. N. Erten, *J. Hazard. Mater.*, 2007, **148**, 761–767.

46 D. J. Yang, Z. F. Zheng, H. Y. Zhu, H. W. Liu and X. P. Gao, *Adv. Mater.*, 2008, **20**, 2777–2781.

47 M. Chávez, L. De Pablo and T. García, *J. Hazard. Mater.*, 2010, **175**, 216–223.

48 K. Savka, Y. Kilivnik, I. Mironyuk, H. Vasylyeva, O. Sych, M. Karbovanets and M. Yevych, *Chem. Phys. Impact*, 2023, **6**, 100151.

49 Y.-M. Zhao, M. Sun, L. Cheng, K.-Y. Wang, Y. Liu, J.-Y. Zhu, S. Zhang and C. Wang, *J. Hazard. Mater.*, 2022, **425**, 128007.

50 A. Modwi, H. Idriss, L. Khezami, A. Albadri, M. Ismail, A. A. Assadi and P. Nguyen-Tri, *Diamond Relat. Mater.*, 2023, **135**, 109830.

51 Y. Liu, F.-Q. Shi, X. Hao, M.-Y. Li, L. Cheng, C. Wang and K.-Y. Wang, *J. Hazard. Mater.*, 2023, **458**, 132038.

52 B.-M. Jun, C. M. Park, J. Heo and Y. Yoon, *J. Environ. Manage.*, 2020, **256**, 109940.

53 J. Gao, S. Fei, Y.-L. Ho, R. Matsuda, H. Daiguji and J.-J. Delaunay, *J. Phys. Chem. C*, 2021, **125**, 17786–17795.

54 S. Fei, A. Alizadeh, W.-L. Hsu, J.-J. Delaunay and H. Daiguji, *J. Phys. Chem. C*, 2021, **125**, 26755–26769.